

Hard X-ray Transient Grating Spectroscopy on Bismuth Germanate - SUPPLEMENTARY MATERIALS

Jérémy R. Rouxel^{1,2,3}, Danny Fainozzi⁴, Roman Mankowsky², Benedikt Rösner²,
Gediminas Seniutinas², Riccardo Mincigrucchi⁴, Sara Catalini⁵, Laura Foglia⁴,
Riccardo Cucini⁶, Florian Döring², Adam Kubic², Frieder Koch², Filippo
Bencivenga⁴, Andre Al Haddad², Alessandro Gessini⁴, Alexei A. Maznev⁷,
Claudio Cirelli², Simon Gerber², Bill Pedrini², Giulia F. Mancini^{1,2,8}, Elia
Razzoli², Max Burian², Hiroki Ueda², Georgios Pamfilidis², Eugenio Ferrari²,
Yunpei Deng², Aldo Mozzanica², Philip J. M. Johnson², Dmitry Ozerov², Maria
Grazia Izzo^{9,10}, Cettina Bottari⁴, Christopher Arrell², Edwin James Divall²,
Serhane Zerdane², Mathias Sander², Gregor Knopp², Paul Beaud², Henrik Till
Lemke², Chris J. Milne^{2,11}, Christian David², Renato Torre⁵, Majed Chergui¹,
Keith A. Nelson⁷, Claudio Masciovecchio⁴, Urs Staub², Luc Patthey², and
Cristian Svetina²

¹Ecole Polytechnique Federale de Lausanne, Laboratory of Ultrafast Spectroscopy (LSU) and
Lausanne Centre for Ultrafast Science (LACUS), CH-1015 Lausanne, Switzerland

²Paul Scherrer Institut, Forschungsstrasse 111, 5232 Villigen, Switzerland

³Univ Lyon, UJM-Saint-Etienne, CNRS, Graduate School Optics Institute, Laboratoire Hubert
Curien UMR 5516, Saint-Etienne F-42023, France

⁴Elettra-Sincrotrone Trieste S.C.p.A., S.S. 14 km 163,5 in Area Science Park, I-34149 Basovizza,
Trieste, Italy

⁵European Laboratory for Non-Linear Spectroscopy (LENS) and Dip. Di Fisica ed Astronomia,
Università degli studi di Firenze, 50019, Sesto Fiorentino, Firenze, Italy

⁶Istituto Officina dei Materiali-CNR, 34149 Basovizza (TS), Italy

⁷Department of Chemistry, Massachusetts Institute of Technology, Cambridge, Massachusetts
02139, USA

⁸Department of Physics, University of Pavia, I-27100 Pavia, Italy

⁹Sapienza Università di Roma, Dipartimento di Ingegneria informatica, automatica e gestionale
Antonio Ruberti, via Ariosto 25 00185 Roma, Italy

¹⁰Istituto Italiano di Tecnologia-Center for Life Nanoscience, Viale Regina Elena, 291, 00161
Roma, Italy

¹¹European XFEL GmbH, Holzkoppel 4, 22869 Schenefeld, Germany

March 3, 2021

Contents

1	Talbot effect with convergent Gaussian beams	2
2	Experimental Setup	5
2.1	Experimental geometry	5
2.2	Diffraction gratings	6
2.3	X-ray pump details	7
2.4	Probe laser details	7
2.5	Detectors	8
3	Theoretical estimation of the BGO phonons	9
4	BGO time trace with 1650 nm π phase grating	9
5	Data Processing	10
5.1	Timing tool corrections	11
5.2	I_0 correction	13
5.3	Stitching	14
5.4	Uncertainty estimation	14
5.5	Efficiency and $\chi^{(3)}$ estimation	15
6	Data Analysis	16
6.1	Signal expression	16
6.2	Data fitting	17

1 Talbot effect with convergent Gaussian beams

Here, we briefly review how to evaluate the Talbot effect for a general 1D transmission grating. More details on the effect can be found in the literature [1]. The calculation is conducted within Fresnel theory of diffraction. First, the grating is described in its Fourier representation:

$$T(x) = \sum_n c_n e^{-ink_G x} \quad (1)$$

where x is the transverse spatial coordinate of the grating and k_G is defined as $\frac{2\pi}{d}$, with d being the gratings' pitch. The coefficients c_n are defined as

$$c_n = \frac{1}{d} \int_{-\frac{d}{2}}^{\frac{d}{2}} T(x) e^{ink_G x} dx \quad (2)$$

with $T(x) = A_1 e^{i\phi_1}$ for $0 < |x| < \frac{ad}{2}$ and $T(x) = A_2 e^{i\phi_2}$ for $\frac{ad}{2} < |x| < \frac{d}{2}$. Here a is the groove ratio, A_1, A_2 and ϕ_1, ϕ_2 are the amplitudes and phases of the grating. The general solution for the coefficients is:

$$c_n = \frac{i}{nk_G} (A_2 e^{i\phi_2} - A_1 e^{i\phi_1}) + i \frac{e^{-in2\pi a}}{nk_G} (A_1 e^{i\phi_1} - A_2 e^{i\phi_2}) \quad (3)$$

For a perfect $\frac{\pi}{2}$ grating, we have $A_1 = A_2 = 1$, $\phi_1 = 0$ and $\phi_2 = \frac{\pi}{2}$ and we get

$$c_n = \frac{1+i}{nk_G} (e^{-in2\pi a} - 1) \quad (4)$$

Assuming the coordinate z at the grating location is z_G , the electric field at the phase grating is given by $E_0(x, z_G)T(x)$, with $E_0(x, z_G)$ being the incident electric field. The electric field at any position after the grating can be calculated by performing a Fresnel propagation defined as:

$$E(x, y, z) = \frac{ik}{2\pi z} e^{-ikz} \iint_{-\infty}^{+\infty} E_0(x', y', z_G) T(x') e^{-\frac{ik(x'-x)^2}{2z}} e^{-\frac{ik(y'-y)^2}{2z}} dx' dy' \quad (5)$$

with k the radiation wavevector equal to $2\pi/\lambda$. Solving the integral for an incident plane wave $E_0(x', y', z_G) = E_0 e^{-ikz}$ and setting the origin at the grating location ($z_G = 0$), we get:

$$E(x, y, z) = E_0 e^{-ikz} \sum_n c_n e^{-ink_G x} e^{\frac{in^2 k_G^2}{2k} z} \quad (6)$$

By defining the Talbot distance $z_T = \frac{2\pi k}{k_G^2} = \frac{2d^2}{\lambda}$, it can be seen that at $z = nz_T$, with $n \in \mathbb{N}$, the electric field displays an interference pattern with the same periodicity as the transmission grating.

For a Gaussian beam the same procedure applies. In this case the Fresnel calculation is more challenging and the Talbot effect leads to interference gratings with smaller/larger pitches with respect to the initial diffraction gratings ones due to the convergence/divergence of the photon beam. By defining the incoming Gaussian beam as

$$G(x, y, z) = A_0 \frac{\omega_0}{\omega(z)} e^{-\frac{x^2+y^2}{\omega(z)^2}} e^{-\frac{ik}{2R(z)}(x^2+y^2)} e^{-ikz} e^{-i\Phi(z)} \quad (7)$$

with ω_0 the beam waist and

$$\omega(z) = \omega_0 \sqrt{1 + \left(\frac{2z}{k\omega_0^2}\right)^2}, \quad R(z) = z \left[1 + \left(\frac{k\omega_0^2}{2z}\right)^2\right], \quad \tan(\Phi(z)) = \frac{2z}{k\omega_0^2} \quad (8)$$

and by performing the Fresnel propagation [2], the final result is

$$E(x, y, z) = A_0 \frac{\omega_0}{\omega(z)} e^{-ik(z+z_G)} e^{-\frac{x^2+y^2}{\omega(z)^2}} e^{-\frac{ik}{2R(z)}(x^2+y^2)} e^{-i(\Phi(z_G)+\Phi(z))} \sum_n c_n e^{-\frac{in^2 k_G^2}{4\alpha(z)} z} e^{\frac{ink_G x}{2\alpha(z)}} \quad (9)$$

$$\text{where } \alpha(z) = \frac{1}{\omega(z_G)^2} + i\frac{k}{2} \left(\frac{1}{R(z_G)} + \frac{1}{z} \right).$$

A schematic of Talbot geometry is displayed in Fig. 1a.

The solution presents two new terms if compared to the plane wave case: the localization and magnification terms. The former accounts for the displacement of the Talbot planes which is not

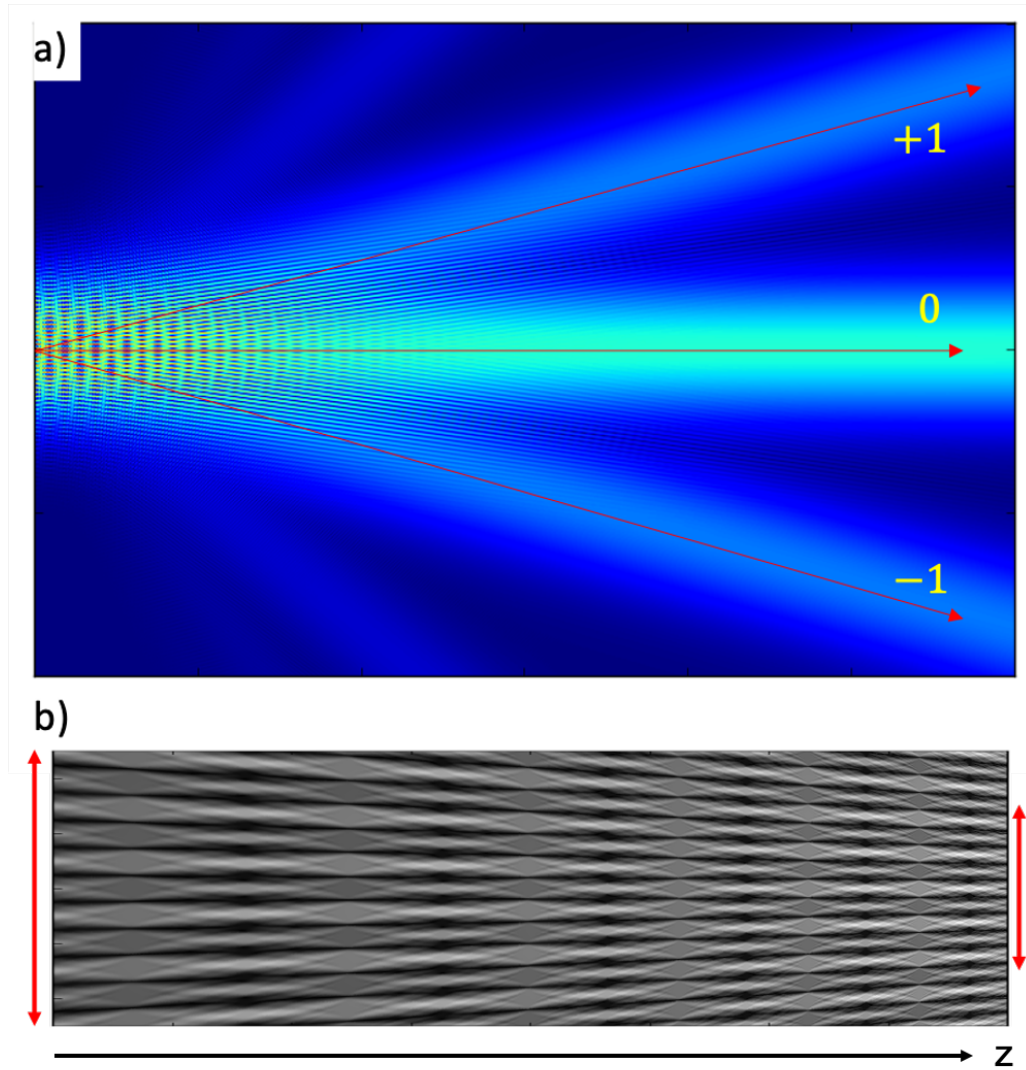


Figure 1: Top, Fresnel simulation of a converging Gaussian beam, coming from the left, diffracted by a transmission grating. Diffraction orders emerge from the grating and interfere generating a Talbot carpet. Bottom, detail of the Talbot carpet for a convergent Gaussian beam generated by a π phase grating. The red arrows indicate the original diffraction grating pitch (left) and the XTG pitch after several Talbot planes. (right).

constant while the second accounts for the pitch of the interference pattern. The latter has the following form:

$$M = \frac{R(z_{Sam})}{R(z_{Sam}) - z^*} \quad (10)$$

where $R(z_{Sam})$ is the radius of curvature at the sample position and z^* is the distance between sample and diffraction grating. It can be seen that, for convergent Gaussian beams, the magnification factor is less than unity. As a consequence, the Talbot interference pattern has a smaller pitch compared to the diffraction grating. A Fresnel simulation displaying this behaviour is shown Fig. 1b.

Another important quantity to be considered is the separation distance, which is the distance from the grating for which the first orders of diffraction stop overlapping. For a Gaussian beam it is:

$$z_{sep} = \frac{w(z_G)}{2 \tan \beta} \quad (11)$$

with β the angle of diffraction of the first orders give by $\arcsin(\frac{\lambda}{d})$ where λ is the wavelength of the radiation.

The calculation starting from Eq. 5 assumed that the beam contains a single wavelength. When considering a pulse having a bandwidth, the Talbot effect occurs for each wavelength and the Talbot planes have a spread along the z -axis. When the bandwidth becomes large enough, the Talbot planes of different orders start to merge; and a continuum is reached. This regime is called the achromatic Talbot effect[3]. In the achromatic Talbot regime, one can position the sample more freely since there is a continuum of interference pattern on the sample, but the fringe visibility (i.e. the XTG efficiency) drops considerably.

In the experimental conditions of the present experiment, the achromatic Talbot effect occurs for the fractional bandwidth of $\Delta\omega/\omega > 15\%$ at the sample position. The FEL SASE beam used in the experiment had a relative bandwidth $\Delta\omega/\omega = 0.3\%$ and thus the achromatic Talbot regime was not reached.

2 Experimental Setup

The XTG experiment presented in the main text relies on the use of diffraction phase gratings to generate the X-ray transient excitation gratings (XTG) on the sample position.

Fig. 2 represents the experimental geometry. The incident FEL beam (in yellow) is diffracted by the phase grating and then impinges on the sample. The Talbot effect generates a transient excitation grating on the sample. A delayed probe laser (in blue) is incident on the sample at the phase matching angle and is diffracted by the excitation grating on the sample. Finally, the diffracted probe is homodyne-detected by a CCD camera.

In the following section, we present the experimental geometry, details on the X-ray pump and optical probe, information on the diffraction gratings and on the detectors.

2.1 Experimental geometry

The incident X-ray beam is focused with bendable KB mirrors (details in section 2.3) and impinges on a phase grating. The Talbot effect creates a periodic pattern (Talbot carpet) at periodic distances

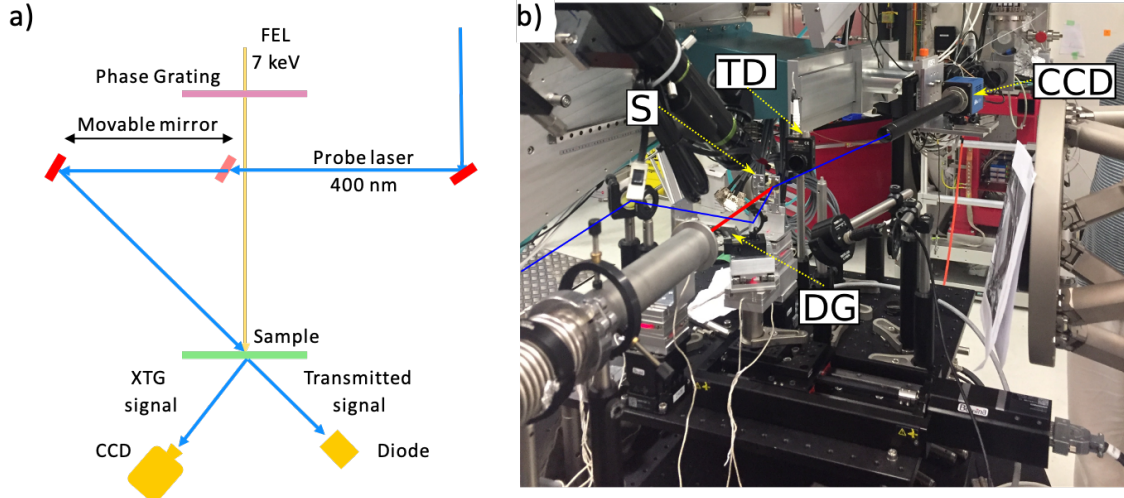


Figure 2: a) Experimental geometry used at Bernina, SwissFEL, to implement the transient grating. b) Annotated picture of the experiment.

(Talbot distances) by the interference of the diffracted orders. Such interferences last only as long as orders of diffraction overlap and set a maximal possible distance between the phase grating and the sample position, usually referred as separation distance (z_{sep}). Moreover, the convergence of the X-ray beam ensures that the excitation grating has a smaller pitch than the phase grating (de-magnification factor) and this pitch is controlled by the X-ray focusing, the distance between the focus and the phase grating and relative distance between grating and sample. For $\frac{\pi}{2}$ phase grating, the transmitted 0th order is present; it also induces some interaction in the sample but it does not contribute to the diffracted XTG signal due to the phase-matching condition. This effect is not present in a perfect π phase grating.

In our experiment the gratings and the sample were mounted on the General Purpose Station (GPS) at Bernina with a separation of 150 mm.

For a π phase grating of 1650 nm pitch, this configuration led to an excitation grating of about 660 nm pitch at the sample position. In this case z_{sep} was about 335 mm while the relative separation of the Talbot planes in the sample area was about 5 mm. For a $\frac{\pi}{2}$ phase grating of 960 nm pitch, the induced excitation grating had a periodicity of 770 nm while z_{sep} and z_t were 240 mm and 1.7 mm respectively.

Formulas giving these parameters for arbitrary diffraction gratings and geometry are given in section 2.2.

2.2 Diffraction gratings

Phase gratings were made of polycrystalline CVD diamond supplied by Diamond Materials GmbH and used to excite transient gratings in the samples. The gratings were fabricated using a similar approach as reported by Makita et al [4]. 10 μm -thick diamond membranes supported by a silicon frame were first cleaned in an $\text{H}_2\text{SO}_4:\text{H}_2\text{O}_2$ 2:1 solution at 120 °C to remove any organic

contamination. Then, the membranes were sputter-coated with a 10 nm thick Cr layer and subsequently spin-coated with $\sim 1 \mu\text{m}$ thick negative tone resist FOX16 followed by baking at 100°C for 3 min on a hotplate. The resist was patterned in an electron beam lithography system (Raith EBPG 5000PlusES) using 100 kV accelerating voltage.

After the exposure, the samples were developed for 8 min in Microposit 351:H₂O 1:3 solution at room temperature, then rinsed in DI water and isopropanol. The patterned resist gratings were hard baked at 300°C for 1 hour on a hotplate to increase etch selectivity between the resist and diamond. The unmasked Cr layer was removed in Cl₂/O₂ plasma revealing the underlying diamond for subsequent etching. Finally, the HSQ grating pattern was transferred into diamond by oxygen plasma etching in an Oxford PlasmaLab 100 machine with the following etching parameters: chamber pressure of 10 mTorr, 30 sccm O₂ flow rate, powers of ICP and RF were 750W and 100W, respectively. After the etching, the remaining mask was stripped in 10% HF solution and the samples cleaned in Cr etchant and an H₂SO₄:H₂O₂ 2:1 solution, followed by rinsing in DI water and isopropanol. A few different pitch gratings were made on one diamond membrane to ease the switching between different gratings during the experiment. Figure 3 shows SEM images of the fabricated gratings. The etch depth for different pitch gratings and samples varied from ~ 3.5 to ~ 6.5 micrometers.

2.3 X-ray pump details

High intensity horizontally polarized X-ray pulses were delivered by SwissFEL with time duration of about 40 fs (rms) and a repetition rate of 50 Hz. The FEL was tuned to 7.1 keV, the emitted radiation had a bandwidth of about 0.3% and was used without a monochromator (pink beam condition) for all the BGO measurements. The FEL beam was focused on a scintillator coupled with a CCD camera through a microscope (X-ray eye) 750 mm downstream the grating by tuning the curvature of the focusing Kirkpatrick-Baez (KB) mirrors. Then, the vertical focus was adjusted to finally obtain an horizontal strip of excitation ($250 \mu\text{m} \times 150 \mu\text{m}$) on the sample matching approximately the size of the non-collinear projection of the optical probe on the sample surface at all phase matching angles. The beam intensity provided by the SwissFEL was ranging from 300 μJ up to 800 μJ while the intensity at the sample was about 1.5 μJ . The phase gratings in the X-ray path were tilted in order to adjust their effective heights and then match the desired phase shift condition.

2.4 Probe laser details

The optical probe laser was generated from a Ti:Sapphire laser delivering 35 fs pulses at 800 nm (10 mJ) and 100 Hz. A Barium borate (BBO) crystal was used to generate the second harmonic (400 nm) with an intensity of about 1.2 μJ . A bandpass filter (40 nm bandwidth) was used to remove the unwanted fundamental harmonic while a waveplate was used to control the intensity. Further filtering was passively done by several bandpass reflecting mirrors. The spot size at the sample was tuned to $190 \times 150 \mu\text{m}^2$ (FWHM) by means of a lens. The arrival time of the probe laser was tuned by a delay stage upstream the sample and the final reflection to the sample was done by a D-shape mirror to accommodate for small phase matching angles. This D-shape mirror was mounted on a linear stage (see Fig. 2) in order to change the phase matching angle when different gratings were being used. The time overlap between the X-ray pump and the optical probe was readjusted for every phase-matching angle.

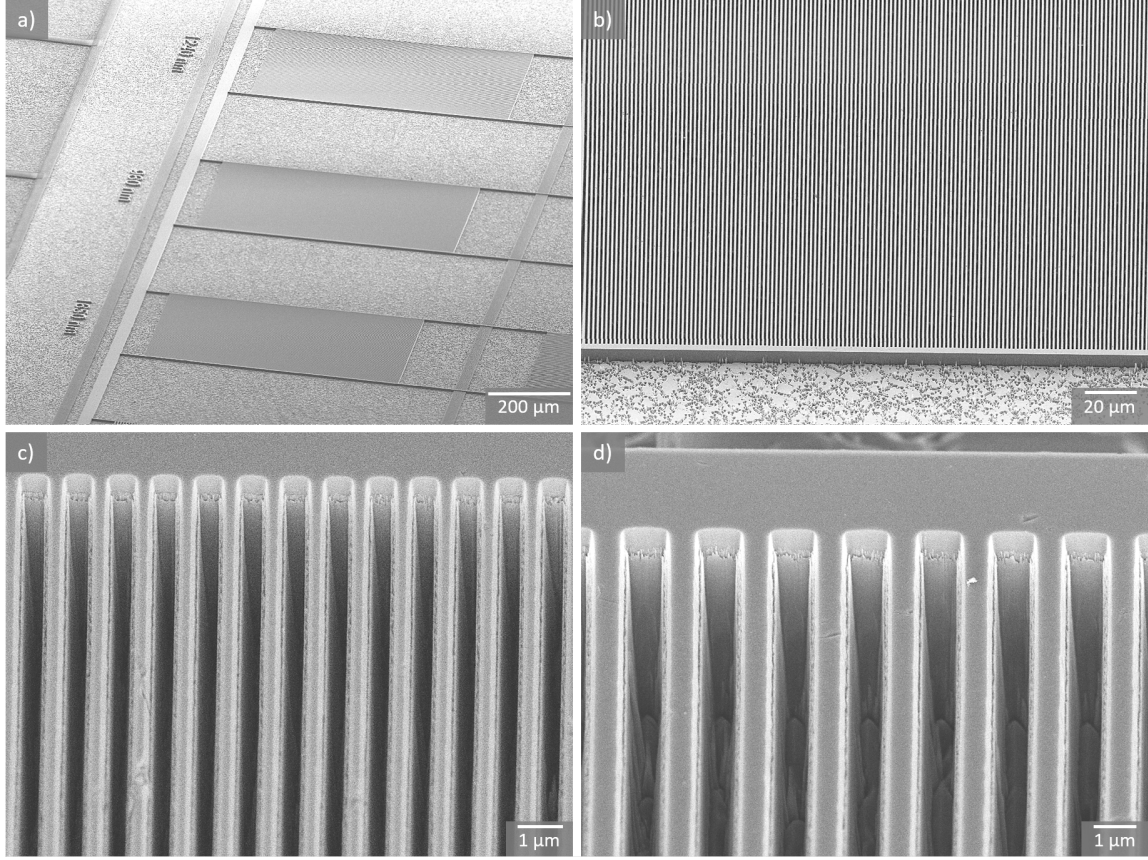


Figure 3: 45-degree-tilt-view SEM images of diamond gratings used in the experiment: a) an overview of diamond membrane with a few gratings; b) closer look at the 1650 nm pitch grating; c) and d) zoomed in images of 960 nm and 1650 nm pitch gratings, respectively.

The optical probe laser operated at twice the repetition rate of the FEL to ensure that no XTG signal was diffracted in the absence of excitation grating on the sample (pumped-unpumped signal). This check ensured that no permanent grating was printed on the sample and that the excitation grating fully relaxed between FEL repetitions. The sample position was kept fixed during the scans unless a permanent imprint was observed.

2.5 Detectors

The optical beams (both in the timing tool and the diffracted XTG beams) were measured by a Charged-Coupled Device (CCD) PCO-edge camera. A 2f-2f lens (200 mm half distance) was installed in front of the CCD imaging the sample at the chip. This allowed to reduce the background at the detector on the CCD camera. In order to control the angle of detection for different phase matching angles, the CCD camera was mounted on an heavy load $\delta - \gamma$ diffractometer at about

800 nm from the sample position and moved in the diffraction plane of the experiment. Then the θ angle was scanned in order to locate the diffracted XTG signal nearby the calculated value.

A typical diffracted XTG spot recorded with the detector is displayed in Fig.4. The signal amplitude was obtained by integrating over the signal area while the weak background was subtracted using an area where the signal is absent. This weak background originated from the isotropic scattering of optical beam from the sample. Dark shots (unpumped signal) were recorded too and used for normalizing the data as well as to check that the sample was not printed during the measurements. The absence of a remnant grating, either from permanent imprinting or from non-relaxed thermal grating from the previous shot, was constantly monitored by analyzing the intermitted shots without x-rays.

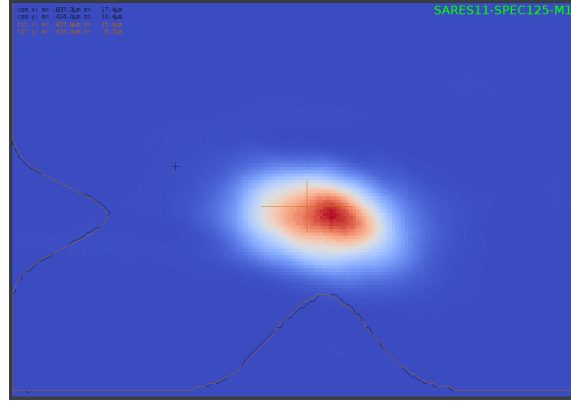


Figure 4: Raw image of the XTG signals on BGO (delay of 1 ps with an excitation grating pitch of 660 nm). The XTG signal is obtained by integration over the diffraction peak for each shot.

Finally, an ultra-fast diode was positioned in transmission along the optical probe path with the purpose to measure the laser transmitted thorough the sample (see Fig.2).

3 Theoretical estimation of the BGO phonons

Phonon calculations were performed by the supercell approach. The initial crystal structure used to perform phonon calculation is obtained from the Materials Project [5]. Phonon frequencies were calculated from the force constants using the PHONOPY code [Phonopy]. For the QHA calculations, supercells containing 2x2x1 unit cells were used. The simulated A_1 optical phonon is 2.609 THz, in excellent agreement with the measured value of 2.605 THz.

4 BGO time trace with 1650 nm π phase grating

In this section, we present XTG measurements on BGO with a 1650 nm pitch π phase grating corresponding to a nominal excitation XTG pitch of about 660 nm. For this measurement, a fast diode was used in transmission to detect the pump-probe signal.

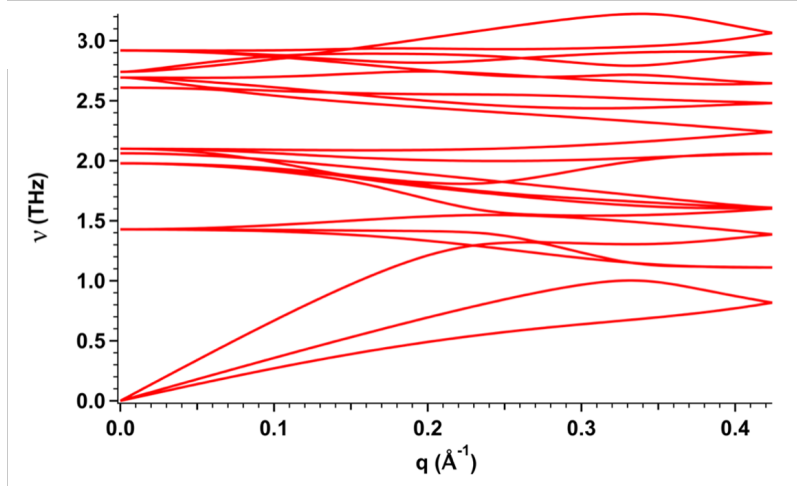


Figure 5: Phonon dispersion along $\Gamma - N$

The short and long XTG time traces are displayed in Fig. 6a and b. The higher noise level compared to the trace shown in the main text is attributed to instabilities of the FEL source during the measurement and the laser incident angle not in a perfect phase matching condition. As for the case reported in the main text, the short time trace displays an exponential ultra-fast decay. By Fourier transforming the residual, see section 6.2, the optical phonon modulation is identified to be equal to 2.6 ± 0.1 THz and is displayed in Fig. 6c.

The long time trace have been fitted with an exponential function and the residuals have been Fourier transformed (Fig. 6 d). The obtained spectrum displays several frequency components at 24.1 ± 0.1 GHz, 47.8 ± 0.3 GHz and $70. \pm 1.$ GHz, similarly to the trace shown in the main text.

The probe laser intensity I_{trans} was recorded in transmission by means of an ultrafast diode. Fig. 7a shows the fast response measured by the diode: the rise time, defined as the σ_{diode} in the $\text{erf}(\frac{t-t_0}{\sigma_{\text{diode}}})$ function used to fit the transient traces, is $\sigma_{\text{diode}} = 159 \pm 13$ fs. As expected, the transmitted signal does not display any signature of the optical phonon during the short time trace. In the long time scale, Fig. 7b, the long lived oscillatory components at 24.0 ± 0.1 GHz, 47.9 ± 0.3 GHz and $70. \pm 1.$ GHz are present.

Since the 24 GHz oscillations are present both in the transmission and the XTG signals, we can assume that they are caused by a modulation of the optical index within the material. To our knowledge such evidence has never been reported. Additional experiments will be carried to understand the nature and underlying mechanism involved in the generation of these frequencies.

5 Data Processing

In this section, we present the data reduction procedure applied to the shot-to-shot raw data. This includes the jitter correction (section 5.1), the intensity normalization (section 5.2) and the stitching of scans acquired over multiple acquisitions.

We also describe how the uncertainties have been calculated (5.4) as well as the XTG efficiency

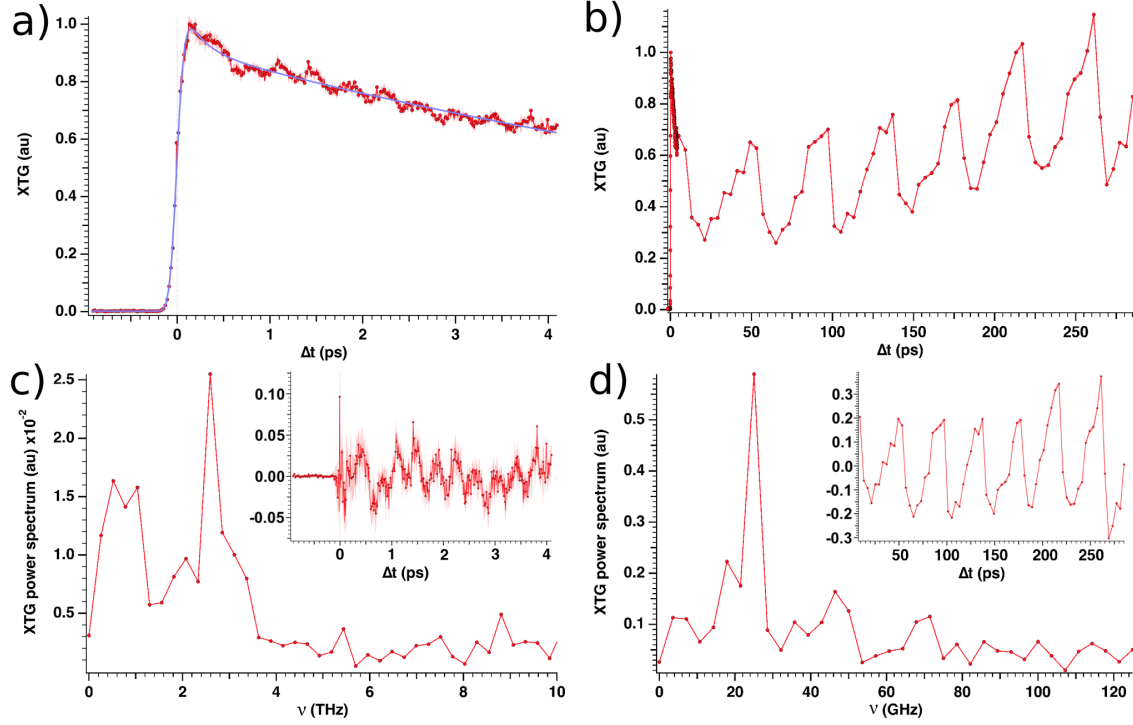


Figure 6: XTG measurements on BGO with a 660 nm excitation grating. a) Short time trace. b) Long time trace. c) Fourier transform of the residual from the fit in Fig. 6a. d) Fourier transform of the residual after subtraction of an exponential function from Fig. 6b.

and $\chi^{(3)}$ estimation (5.5).

5.1 Timing tool corrections

Self Amplified Spontaneous Emission (SASE) FELs do not take advantage of external seed lasers. As a consequence, the pump (or probe) laser is an independent system synchronized with the FEL timing system. Nevertheless, the relative arrival time between the pump (or probe) laser compared to the FEL beam is affected by short term fluctuations (jitter) which can be as high as hundred of femtoseconds affecting the overall time resolution. The jitter is usually measured by means of dedicated diagnostics systems, named timing tools, such as Spatial Encoding, Spectral encoding and Terahertz streaking methods, which provide the relative arrival time on a shot-to-shot basis. During our experiment we have taken advantage of a spatial encoding timing tool which relies on the ultrafast induced transparency of a screen by the interaction with the X-rays. By impinging a portion of the laser on the screen with an angle and measuring the transmitted laser beam with a CCD camera. In this way different horizontal pixels in the CCD camera correspond to different relative arrival times between the X-ray and optical pulses. By measuring the variation in position of the ultrafast change of the transmitted signal it is then possible to retrieve the jitter for each shot

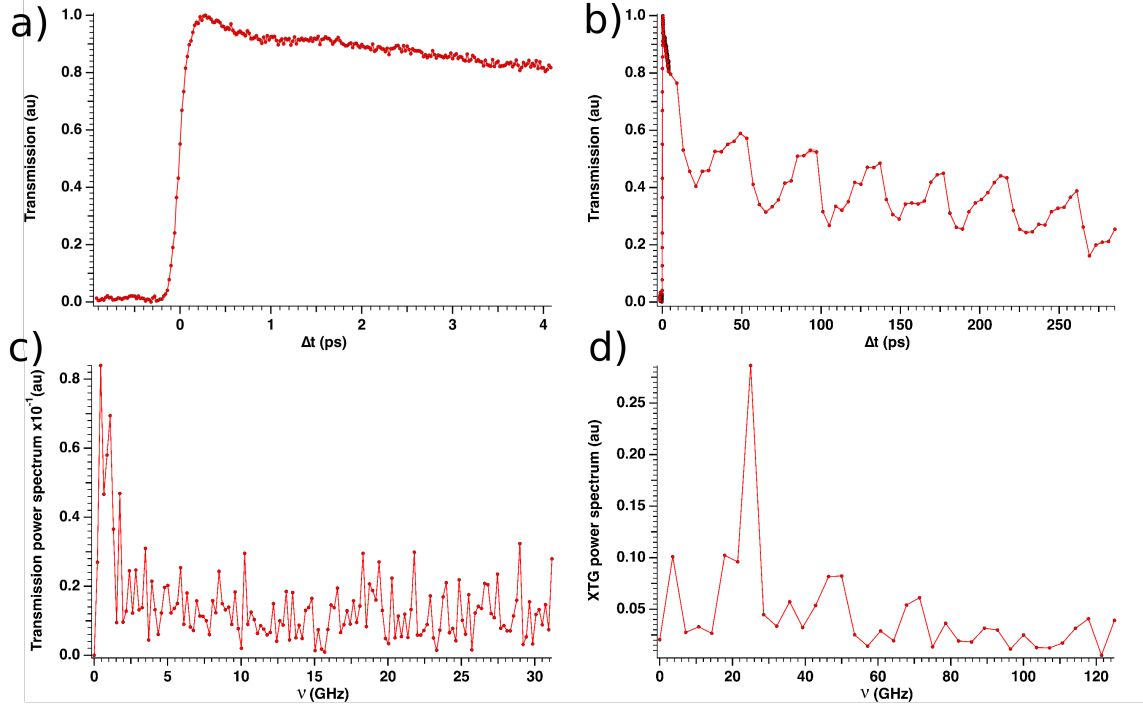


Figure 7: Transient absorption on BGO with a 660 nm excitation grating (diffraction grating pitch of 1650nm). a) Short time component. b) Long time trace. c) Fourier transform of the residual from the fit in Fig. 7a. d) Fourier transform of the residual from the fit in Fig. 7b.

and to normalize the data with a resolution down to few femtoseconds.

We used a Ce:YAG screen positioned right after the KB mirrors and a portion of the optical pump laser was directed on the screen (45 deg incidence angle) and monitored by a PCO Edge 5.5 camera. The expected resolution is about 2.65 fs/pixel.

For each shot, the CCD camera array was vertically binned and resulted in traces similar to the one presented in Fig. 8a. To find the center of the rising slope, each trace was fitted using a polynomial function (blue curve in Fig. 8a). Then, the resulting polynomial was derived and its maximum was used as the rising slope center value (see Fig. 8b).

For each scan, the Gaussian-like distribution of these pixel values Δp_i was shifted by its mean following the relation $\Delta p_i \rightarrow \Delta p_i - \frac{1}{n} \sum_n \Delta p_n$. A calibration of the timing tool provided a conversion rate between pixels on the CCD and their time delays Δt_i^{tt} in fs/pixel. These obtained jitter values were then added to the pump-probe delay Δt_{pp} set by the delay stages for each shot to obtain their timing tool corrected delays $\Delta t_i = \Delta t_{pp} + \Delta t_i^{tt}$.

Finally, the data was re-binned using the timing tool corrected data, leading a largely increased time resolution limited by the pulses lengths instead of the time jitter. In Fig. 9, we display the XTG signal for a 770 nm excitation grating before and after the timing tool correction.

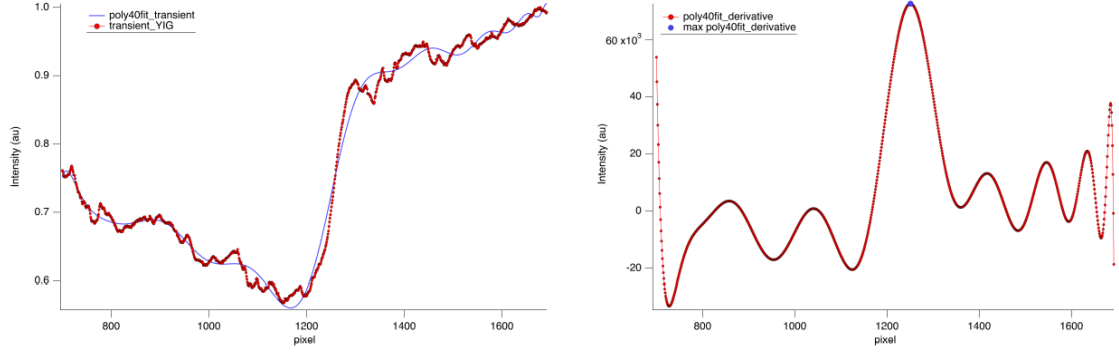


Figure 8: Left: Vertical binning of a single transmitted optical beam on the PCO and its polynomial fit. The slope indicates a change of transmission induced by the coincident X-ray pulse. Right: derivative of the polynomial fit. Its maximum point provides an accurate measurement of the center of the slope while its variation is a good estimate of the time jitter. The pixel/fs conversion is done by an independent calibration of the timing tool.

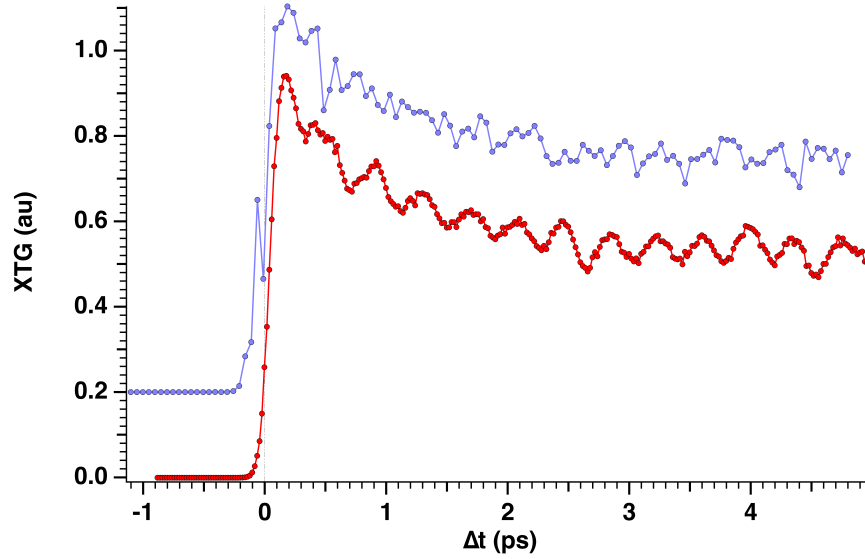


Figure 9: Blue: XTG signal before timing tool correction. Red: After the timing tool correction. The blue curve has been vertically shifted for the display.

5.2 I_0 correction

The XTG and diode signals were also normalised respect to the incoming FEL intensity on a shot-to-shot basis. Each FEL shot intensity was measured using the photon beam position monitor (PBPS) of SwissFEL[6] made of a thin 200 nm Si_3N_4 membrane that back-scatters a small portion

of the incoming beam onto four diodes. The mean signal on the four diodes was used to deduce the I_0 incoming pulse intensity.

The XTG signal scales as

$$I_{\text{XTG}} \propto |\chi^{(3)}|^2 I_{\text{XFEL}}^{-1} I_{\text{XFEL}}^{+1} I_{\text{laser}} \quad (12)$$

where $I_{\text{XFEL}}^{\pm 1}$ is the intensity of the two XFEL diffracted ± 1 orders, I_{laser} is the intensity of the probe laser and $\chi^{(3)}$ is the third order susceptibility of the system.

The I_{laser} jitter was negligible during the acquisition. Moreover, the $I_{\text{XFEL}}^{+1} = I_{\text{XFEL}}^{-1}$ intensities are proportional to the total FEL intensity $I_{\text{FEL}}^{\pm 1} = \theta I_{\text{FEL}}$ with θ being the efficiency of the diffractive zone plate. The I_0 correction on the experimental XTG signal was thus calculated as:

$$I_{\text{XTG}} = \frac{I_{\text{XTG}}^{\text{exp}}}{I_0^2} \quad (13)$$

5.3 Stitching

Some traces were acquired over multiple scans due to various FEL instabilities. These traces had to be stitched together to provide a full time trace, taking in account some changes in the FEL parameters, in particular shifts in the mean value of I_{XFEL} .

We took into account this shift by stitching our traces considering the time overlap and adjusting the intensity using the proportionality condition expected by equation (12) and (13). Considering the mean value of I_0 moving to $I_0 + \Delta I_0$ in two subsequent scans, we expect the shift ΔI_{XTG} of the signal to be

$$\frac{I_{\text{XTG}}}{I_0^2} = \frac{I_{\text{XTG}} + \Delta I_{\text{XTG}}}{(I_0 + \Delta I_0)^2} \implies \Delta I_{\text{XTG}} = I_{\text{XTG}} \left[\frac{(I_0 + \Delta I_0)^2}{I_0^2} - 1 \right] \quad (14)$$

5.4 Uncertainty estimation

The uncertainty estimation was evaluated as a type A uncertainty within each bin after the time tool correction. In each time bin, the standard deviation was evaluated and used as an uncertainty in subsequent analyses.

Data curve fittings were weighted by the uncertainty to give more weights to the points with the lowest uncertainties. This procedure provided fitting parameters with a much lower estimated standard deviation on them (see section 6.2.)

All errors bar in the main text and Supplementary Materials are displayed as a ± 1 s.e.m. interval around the mean.

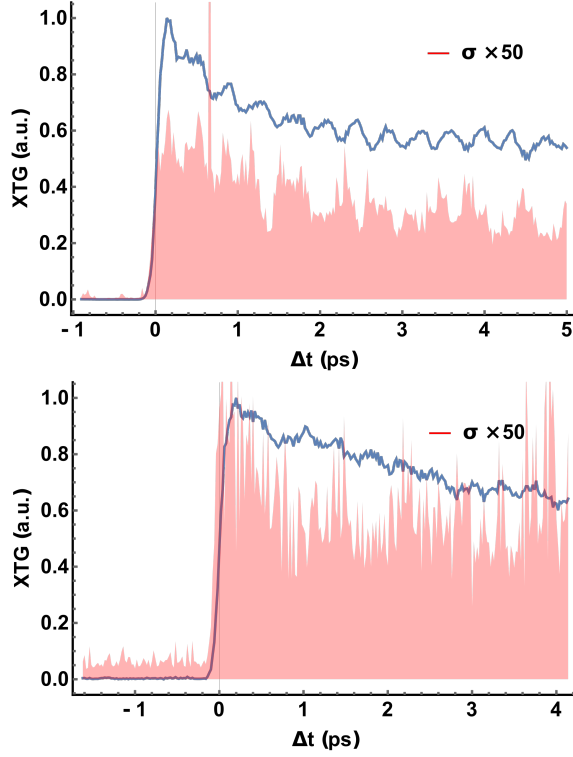


Figure 10: Display of the type A uncertainty of the XTG time traces. σ is the standard deviation of the data within each time bin and has been scaled by a factor of 50 to compare with the data absolute amplitude. Top: short time traces with a XTG pitch of 660 nm. Bottom: Same with a 770 nm XTG pitch.

5.5 Efficiency and $\chi^{(3)}$ estimation

Following the procedure given by [7] we estimated the efficiency η_{eff} of the XTG process and the susceptibility value at the electronic peak. The efficiency was calculated as the ratio between the incoming probe intensity I_{laser} and the outgoing XTG signal intensity $\eta_{\text{eff}} = \frac{I_{\text{probe}}}{I_{\text{XTG}}} = 1.3 \times 10^{-4}$. The $\chi_{\text{eff}}^{(3)}$ value was estimated using its classical definition, which can be expressed for our configuration as follow[8]

$$P_{\text{XTG}} = \epsilon_0 \chi_{\text{eff}}^{(3)} E_{\text{XFEL}}^{-1} E_{\text{XFEL}}^{+1} E_{\text{probe}} \quad (15)$$

where P_{XTG} is the XTG nonlinear polarization, $E_{\text{XFEL}}^{\pm 1}$ is the field amplitude of the two XFEL pumps ± 1 orders and E_{laser} is the electric field of the probe laser. The detected signal amplitude is given by

$$\frac{\partial E_{\text{XTG}}(z, t)}{\partial z} = -i \frac{\omega_{\text{probe}}}{2\epsilon_0 c n_{\text{probe}}} P_{\text{XTG}}(t) e^{i\Delta k z} \quad (16)$$

Upon integration over the thickness of the transient grating in the sample ($L = 6\mu\text{m}$), the emitted field amplitude is:

$$E_{\text{XTG}}(t) = i \frac{\omega_{\text{probe}}}{2\epsilon_0 c n_{\text{probe}}} P_{\text{XTG}}(t) L e^{i\Delta k L/2} \text{sinc}(\Delta k L/2) \quad (17)$$

The detected signal is finally given by

$$I_{\text{XTG}}(t) = \frac{\epsilon_0 c n}{2} |E_{\text{XTG}}(t)|^2 = \frac{\pi^2}{2n_{\text{probe}} Z_0} |\chi_{\text{eff}}^{(3)} I_{\text{XFEL}} I_{\text{probe}}^{1/2} \frac{L}{\lambda_{\text{probe}}} \text{sinc}(\Delta k L/2)|^2 \quad (18)$$

where Z_0 is the impedance of free space. To get to the electric field value expressed in V/m starting from an intensity measurement in μJ we first converted the intensity $I[\mu\text{J}]$ into a more suitable form following the relation

$$I[\text{W m}^{-2}] = \frac{I[\mu\text{J}]}{\Delta t \sigma_x \sigma_y} \quad (19)$$

Where Δt is the time duration of the event which we set equal to the rise time σ_{XTG} and $\sigma_{x/y}$ is the x/y dimension of the overlap between pump and probe on the sample which were $250\mu\text{m}$ and $150\mu\text{m}$ respectively. We estimated the electric field values to be $E_{\text{XFEL}}^{\pm 1} = 5.86 \cdot 10^8 \text{ V/m}$ and $E_{\text{probe}} = 5.14 \cdot 10^{11} \text{ V/m}$, thus leading to the susceptibility value

$$\chi_{\text{eff}}^{(3)} = 2.6 \cdot 10^{-15} \text{ m}^2/\text{V}^2 \quad (20)$$

6 Data Analysis

6.1 Signal expression

A general homodyne-detected signal can be written as [8]:

$$S_{\text{hom}}(\Gamma) = 2F_2(\Delta\mathbf{k}) \left| \int d\omega_s dt e^{i\omega_s t} \langle \boldsymbol{\mu}(t) \rangle \right|^2 + 2N\Re \int dt dt' e^{i\omega_s(t-t')} \langle \boldsymbol{\mu}_L(t) \boldsymbol{\mu}_R(t') \rangle \quad (21)$$

where $F_2(\Delta\mathbf{k}) = N(N-1)\delta(\mathbf{k}_s \pm \mathbf{k}_3 \pm \mathbf{k}_2 \pm \mathbf{k}_1)$ ensures the phase-matching condition and N is the number of scatterers contributing to the signal. Γ is the full set of experimental parameters on which the homodyne signal depends on (central frequencies and time of arrival of the different incoming pulses, etc), $\boldsymbol{\mu}$ is the electric dipole operator.

In the condensed phase, the second term of the signal can be neglected compared to the first one because N is large (on a scale similar to the Avogadro number). The XTG signal is detected by placing the detector in the phase matching direction $\mathbf{k}_s = \mathbf{k}_3 - \mathbf{k}_2 + \mathbf{k}_1$:

$$S_{\text{XTG}}(\Delta t, \mathbf{k}_s = \mathbf{k}_3 - \mathbf{k}_2 + \mathbf{k}_1) = 2N^2 \mathcal{E}_s^2 \left| \int d\omega_s dt e^{i\omega_s t} \mathbf{P}_{\text{XTG}}^{(3)}(t, \Delta t) \right|^2 \quad (22)$$

where $\mathbf{P}_{\text{XTG}}^{(3)}(t, \Delta t)$ is the third-order nonlinear polarization that depends parametrically on the time delay Δt between pump and probe pulses. The first two interactions are the X-ray pulses

with wavevector k_1 and $-k_2$ that generate the transient grating. Immediately after the X-ray excitations, the sample experiences a rapid relaxation process that refills the core-hole and induces low-energy electronic excitations. In turn, the lattice responds to the charge motion caused by these low-lying electronic states and phononic excitations are thus triggered. Most of the relaxation after the X-ray interaction is not resolved in the present experiment and only the subsequent vibrational dynamics is observed.

Explicit expressions of the signal in terms of operator matrix elements can be obtained by expanding the nonlinear polarization over states. In this case, the nonlinear polarization is usually well-described by diagrammatic approaches[8]. Relaxation dynamics observed in the XTG signal are contained in the matter propagator between the X-ray pumps and the optical probe. Full X-ray transient grating measurements with a high time resolution could be expected to also gain information on the core dynamics.

6.2 Data fitting

Considerations from the previous section allow us to define the following model to represent the XTG measured data.

$$S_{\text{XTG}} = \left| \frac{1}{2} \left(1 + \operatorname{erf} \left(\frac{t - t_0}{\sigma} \right) \right) \left(c_1 e^{-\frac{(t-t_0)}{t_1}} + c_2 e^{-\frac{(t-t_0)}{t_2}} \cos(2\pi\nu_2(t - t_0)) + c_3 \right) \right|^2 \quad (23)$$

We account for overdamped oscillation by adding two exponential decays t_1 and t_2 . The known optical phonon at 2.6 THz is assigned to the damped oscillation terms with frequency ν_3 . Finally, t_0 and σ are experimental parameters accounting for the time zero shift from arbitrary units to the absolute time zero of the time trace and for the instrument response function respectively.

The short time traces are fitted with Eq. 1 of the main text and the resulting fitting parameter are given in Table 1 and 2.

For convenience, we recall Eq. 1 of the main text:

$$S_{\text{XTG}} = \left| \frac{1}{2} \left(1 + \operatorname{erf} \left(\frac{t - t_0}{\sigma} \right) \right) \left(c_1 e^{-\frac{(t-t_0)}{\tau}} + c_2 \right) \right|^2 \quad (24)$$

	c_1	c_2	c_3	t_1 (ps)	t_2 (ps)	t_0 (ps)	σ (ps)
estimate	0.7	0.25	0.74	0.04	1.05	0.05	0.08
standard error	0.1	0.01	0.01	0.01	0.05	0.01	0.01

Table 1: Fit parameters on the short XTG time trace of BGO, using Eq. 1 in the main text, with an excitation grating pitch of 770 nm.

Finally, Table 3 provides a summary of all frequencies appearing in the signal and their corresponding uncertainty for an excitation grating with a 660 nm pitch.

Standard errors in Tables 1 to 3 are obtained from the fitting routine and indicates the quality of the fit to the experimental time trace. They are, however, not an indication of the experimental uncertainty of these parameters.

In Fig. 11, we display a fit of the whole dataset using Eq. 23 and by fixing the fast time scales using the results in Table 1 (for the fast response) and the frequency components obtained from

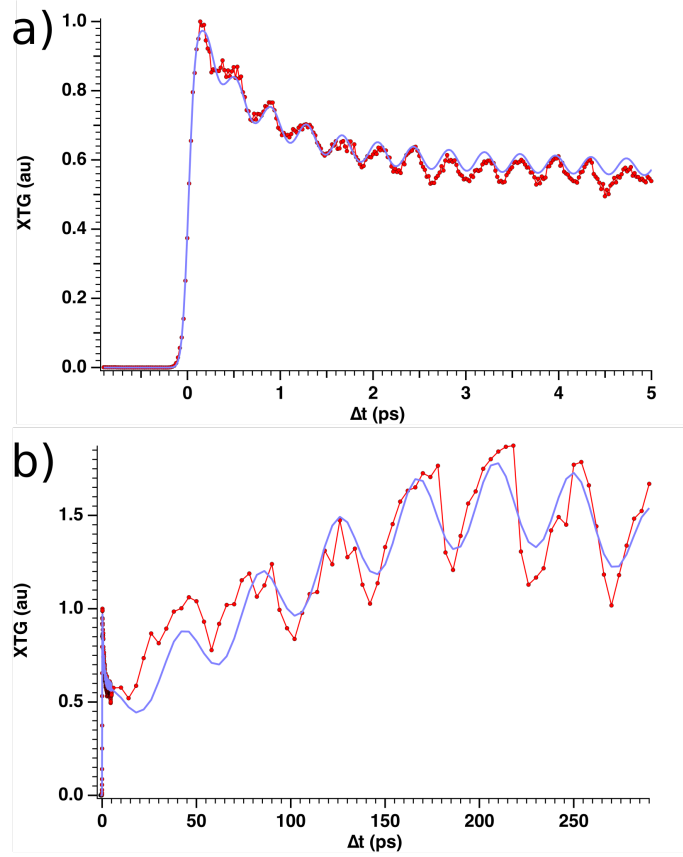


Figure 11: Global fit of the data with Eq. 23. The short lifetimes have been fixed by a fit on the short time trace, the fast and long modulation are fixed at the maximum of the Fourier transform of the residuals and the low frequency modulation is fixed to the value obtained from optical measurements.

	c_1	c_2	c_3	t_1 (ps)	t_2 (ps)	t_0 (ps)	σ (ps)
estimate	0.91	0.37	0.60	0.05	6.	0.10	0.10
standard error	0.03	0.05	0.05	0.01	1.	0.01	0.01

Table 2: Fit parameters on the short XTG time trace of BGO, using Eq. 1 in the main text, with an excitation grating pitch of 660 nm.

the Fourier transform of the residuals including the longitudinal acoustic phonon as well as the additional frequencies seen also in transmission. In the fit only the c components were kept as free parameters.

	ν_3 (THz)	ν_4 (GHz)	ν_5 (GHz)	ν_6 (GHz)	ν_7 (GHz)
estimate	2.61	6.	23.5	47.4	70.
standard error	0.01	1.	0.1	0.4	1.

Table 3: Frequencies extracted from the XTG data obtained on BGO with a 660 nm pitch excitation grating. ν_3 is the optical phonon of BGO, ν_4 its longitudinal phonon, ν_5 , ν_6 and ν_7 are the frequencies obtained by Fourier analysis of the long time trace. Uncertainties of frequencies ν_3 , ν_5 and ν_6 have been obtained from fitting the data with a sine function while uncertainties on ν_4 and ν_7 have been computed from the standard deviation of the Fourier peak since their residuals are too weak for the fit to be accurate.

References

- [1] Paul Latimer and Randy F Crouse. “Talbot effect reinterpreted”. In: *Applied optics* 31.1 (1992), pp. 80–89.
- [2] S Szapiel and K Paturski. “Fresnel diffraction images of periodic objects under Gaussian beam illumination”. In: *Optica Acta: International Journal of Optics* 26.4 (1979), pp. 439–446.
- [3] Nicolas Guérineau, Bouchra Harchaoui, and Jérôme Primot. “Talbot experiment re-examined: demonstration of an achromatic and continuous self-imaging regime”. In: *Optics communications* 180.4-6 (2000), pp. 199–203.
- [4] Mikako Makita et al. “Fabrication of diamond diffraction gratings for experiments with intense hard x-rays”. In: *Microelectronic Engineering* 176 (2017), pp. 75–78.
- [5] Anubhav Jain et al. “Commentary: The Materials Project: A materials genome approach to accelerating materials innovation”. In: *Apl Materials* 1.1 (2013), p. 011002.
- [6] Christopher J Milne et al. “SwissFEL: the Swiss X-ray free electron laser”. In: *Applied Sciences* 7.7 (2017), p. 720.
- [7] F Bencivenga et al. “Four-wave mixing experiments with extreme ultraviolet transient gratings”. In: *Nature* 520.7546 (2015), pp. 205–208.
- [8] Shaul Mukamel. *Principles of nonlinear optical spectroscopy*. Vol. 6. Oxford university press New York, 1995.